Aveiro, H. C., Hysell, D. L., Park, J., Lühr, H. (2011): Equatorial spread F-related currents: Three-dimensional simulations and observations. - Geophysical Research Letters, 38, L21103

DOI: 10.1029/2011GL049586

Equatorial spread *F*-related currents: Three-dimensional simulations and observations

H. C. Aveiro,[1] D. L. Hysell,[1] J. Park,[2] and H. Lühr[2]

Received 6 September 2011; revised 4 October 2011; accepted 4 October 2011; published 4 November 2011.

[1] A three-dimensional numerical simulation of plasma density irregularities in the postsunset equatorial *F* region ionosphere leading to equatorial spread *F* (ESF) is described. Simulated satellite passes are compared with CHAMP magnetometer observations. The comparisons imply that magnetic perturbations parallel to the main field are mainly due to diamagnetic currents flowing on the external walls of the plasma depletions. The divergence of the transverse currents generate field-aligned currents flowing poleward (equatorward) on the external edges of the western (eastern) walls of the depletions which are furthermore detectable in the transverse magnetic field components. That the simulation is electrostatic argues against an Alfvénic interpretation of all of the CHAMP magnetic field observations in ESF. **Citation:** Aveiro, H. C., D. L. Hysell, J. Park, and H. Lühr (2011), Equatorial spread *F*-related currents: Three-dimensional simulations and observations, *Geophys. Res. Lett.*, *38*, L21103, doi:10.1029/2011GL049586.

1. Introduction

[2] Equatorial spread *F* (ESF) refers collectively to a family of plasma irregularities that form in the equatorial *F* region ionosphere after sunset. ESF has been extensively studied with support of coherent scatter radars, ionosondes, airglow imagers, ground-based scintillation receivers, and instruments onboard rockets and satellites (see, e.g., *Woodman* [2009] for a complete review of observations). Among those, magnetometers are the only instruments able to measure perturbations in the ionospheric current system. In the last two decades, experimental evidence of magnetic perturbations associated with ESF has been shown by magnetometers onboard the San Marco-D and AE-2 [*Aggson et al.*, 1992], CRRES [*Koons et al.*, 1997], CHAMP [*Lühr et al.*, 2002], and DEMETER satellites [*Pottelette et al.*, 2007]. *Bhattacharyya and Burke* [2000], using a transmission line analogy, explained those magnetic perturbations in terms of field-aligned currents (FAC) generated by equatorial *F* region irregularities. Experimental observations made by the DEMETER satellite support this idea [*Pottelette et al.*, 2007].

[3] To evaluate how the electric current loop closes in the presence of those plasma depletions, we perform three-dimensional simulations of ESF under realistic conditions. We then compute the magnetic perturbations due to currents in the presence of well-developed depletions with the help of a diagnostic code based on Ampère's law. ESF development and morphology are validated against ALTAIR radar data, and the magnetic perturbations are compared to CHAMP satellite data. The simulation is based on an electrostatic potential solver which enforces the divergence-free current constraint. The scheme does not include any electromagnetic features (i.e., Alfvén waves are not part of the system).

[4] The main issue we address here is the degree to which it is possible to predict the current densities related to ESF and their relative contributions to space-based magnetometer measurements given an appropriate specification of the initial conditions and the forcing.

2. Radar Observations

[5] We begin with a presentation of radar observations in the Pacific sector that will ultimately be used to motivate and validate the numerical simulations. The ARPA Long-Range Tracking and Instrumentation Radar (ALTAIR) is a VHF/UHF radar located at Kwajalein Atoll (8.8°N, 167.5°E). ALTAIR observations made perpendicular to the geomagnetic field at *F* region heights represent a combination of coherent and incoherent scatter, whereas off-perpendicular scans reflect only incoherent scatter. Both can be useful ESF diagnostics.

[6] The radar observations described below were used to guide the numerical simulations in terms of ESF development and morphology. Figure 1 displays ALTAIR UHF (422 MHz) data for the night of August 11, 2004, acquired during the EQUIS II rocket campaign [*Hysell et al.*, 2006]. By 10:39 UT (Figure 1, top), a meridional scan revealed the presence of multiple depleted flux tubes. Note how one of the anomaly crests interacted with the plasma depletions north of the radar site. By 10:50 UT (Figure 1, bottom), a perpendicular (to the geomagnetic field) scan showed a quasi-periodic train of large-scale depletions spaced by 100–200 km and tilted westward.

3. Numerical Simulations

[7] The simulation described here is cast on a coordinate system based on the mean magnetic field: "ϕ" and "L" denote directions perpendicular to the magnetic meridian and point eastward (zonal) and outward (meridional), respectively, whereas "$\|$" represents quantities along the mean field. The model uses a rectangular grid 139 × 189 × 133 points wide in (L, ϕ, $\|$) space. A cut through the equatorial plane spans altitudes between 90–510 km and longitude excursions between ± 6°. The flux tubes covered by the parallel coordinate all extend to the lower *E* region.

[1]Earth and Atmospheric Sciences, Cornell University, Ithaca, New York, USA.
[2]Helmholtz Center Potsdam, GFZ German Research Center for Geosciences, Potsdam, Germany.

0094-8276/11/2011GL049586

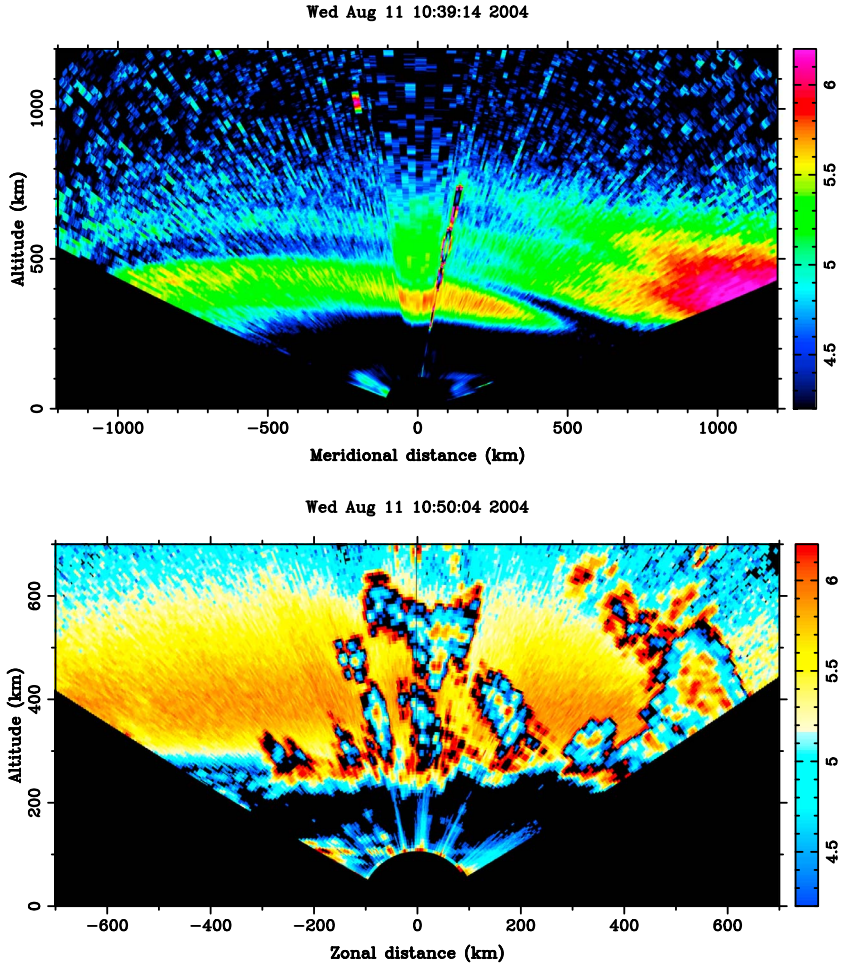

Figure 1. ALTAIR radar scans for August 11, 2004, showing backscatter power, range corrected and scaled to electron density on a logarithmic scale: (top) meridional scan by 10:39 UT and (bottom) perpendicular scan by 10:50 UT (LT ≈ UT + 11 hr for the Kwajalein sector).

The simulation updates ion density and electrostatic potential in time based on the requirements of quasineutrality, continuity equation and momentum conservation. Inertia is neglected in the present incarnation. We take the ionosphere and neutral atmosphere to be in thermodynamic equilibrium after sunset ($T_n = T_e = T_i$). The runs shown below are centered on the dip equator near Kwajalein (5.5° N latitude, 166.5° E longitude, 7.4° declination) with background conditions modeled for August 11, 2004. To seed the simulation run, we added independent Gaussian white noise to the initial number density.

3.1. Model Description

[8] The simulation algorithm performs two computations. First, the self-consistent electric field is found using a 3-D potential solver based on the solenoidal current condition:

$$\nabla \cdot \left[\hat{\Sigma} \cdot \nabla \Phi\right] = \nabla \cdot \left[\hat{\Sigma} \cdot (\mathbf{E}_o + \mathbf{U} \times \mathbf{B}) + \hat{D} \cdot \nabla n + \hat{\Xi} \cdot \mathbf{g}\right] \quad (1)$$

where $\mathbf{E}_o$ is the background electric field, $\hat{\Sigma}$ is the conductivity tensor, $\hat{D}$ includes the diffusivity tensor, $\hat{\Xi} \cdot \mathbf{g}$ is gravity-driven current density, and Φ is the electrostatic potential that must arise to preserve a divergence-free current density. Equation (1) is derived based on the steady-state force balance of the plasma and explicit definitions of the tensors are given by *Shume et al.* [2005]. Equation (1) is solved using the BiConjugate Gradient Stabilized (BiCG-Stab) method using the algorithms described by *Saad* [1990]. We neglect diamagnetic currents here, since their associated flux divergence is very small compared to the other terms [see, e.g., *Aggson et al.*, 1992]. Second, ion velocities are obtained from the momentum equation (inertia is neglected in the present incarnation) and we solve a discretized version of continuity equation for each ion species using a monotone upwind scheme for conservation laws (MUSCL) [e.g., *Trac and Pen*, 2003].

[9] To initialize the model runs, densities and temperatures were derived from empirical models (see *Aveiro and Hysell* [2010] for a more complete description of the inputs). We took the ionosphere and neutral atmosphere to be in thermodynamic equilibrium after sunset. The forcing due to the zonal background electric field was based on the Scherliess-Fejer model [*Scherliess and Fejer*, 1999]. For our runs, only the zonal neutral winds were considered. These were based on profiles measured during the EQUIS II sounding rocket campaign (August 7, 2004) between 100–150 km. Lacking wind measurements above 150 km, we made use of the Horizontal Wind Model (HWM-07) above 200 km altitude. For altitudes in between, the wind profiles were joined smoothly by a continuous function.

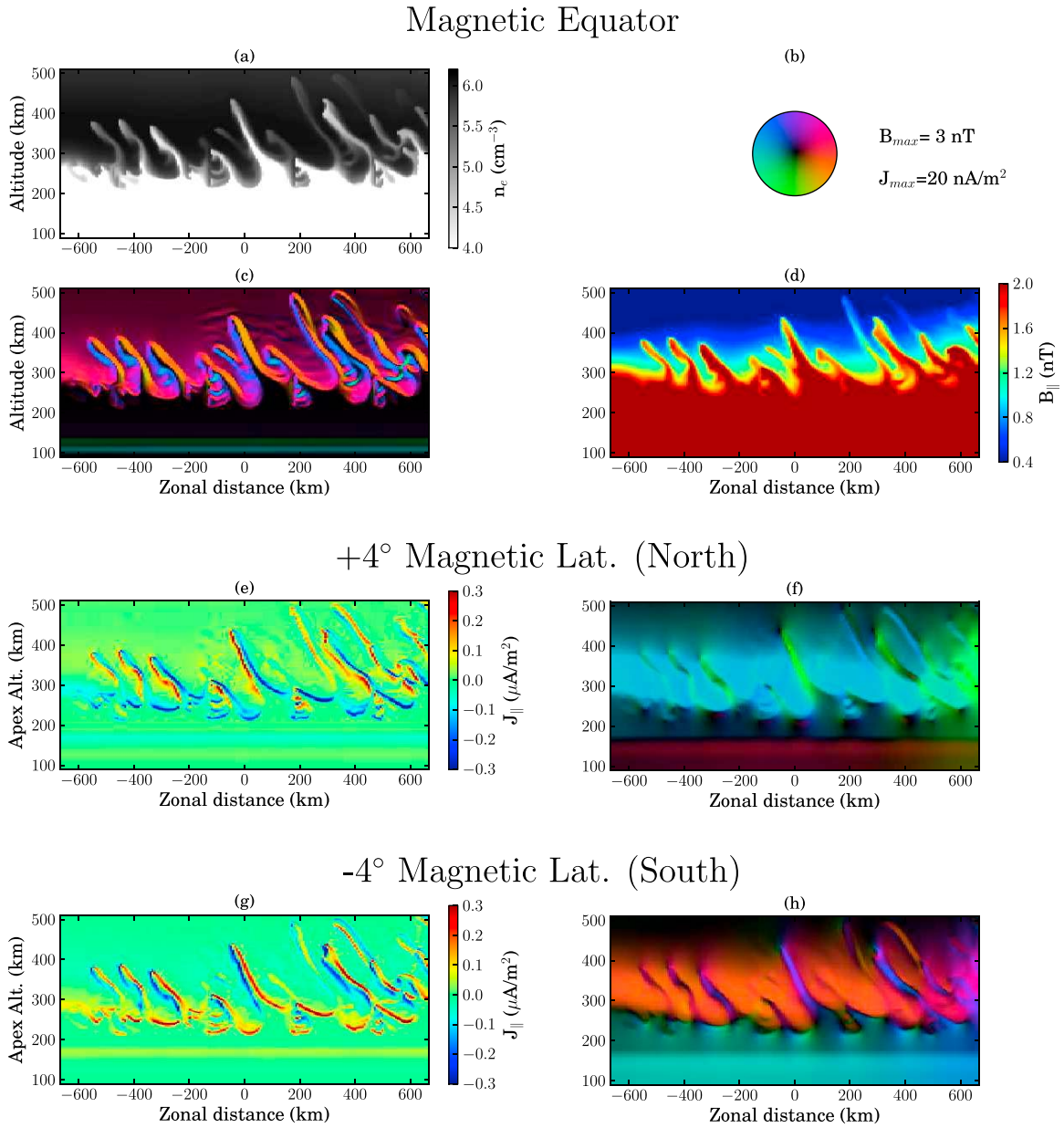

Figure 2. Diagnostic at 10:24 UT: (a) plasma density in a cut through the equatorial plane on a log scale, (b) color scale of the magnitude and direction of the transverse current densities (scale maximum is 20 nA/m^2) and transverse magnetic inductions (scale maximum is 3 nT), (c) transverse current densities and (d) parallel magnetic induction in the equatorial plane, (e) parallel current density and (f) transverse magnetic induction at 4° mag. latitude, and (g) parallel current density and (h) transverse magnetic induction at −4° mag. latitude.

[10] To compute the magnetic induction due to ionospheric currents, we used Ampère's law ($\nabla \times \mathbf{B} = \mu_0 \mathbf{J} + \mathbf{E}/c^2$). Contributions from the Earth's magnetic field can be neglected since the simulations were built on a magnetic dipole field, which is irrotational. Note that, despite being neglected during the computation of the electrostatic potential, diamagnetic currents ($= \Sigma_\alpha d_{H\alpha} \nabla n_\alpha \times \hat{\mathbf{q}}$, where $\alpha = O^+, NO^+, O_2^+$, and electrons) are included in the diagnostic computation of the magnetic field perturbations (see *Shume et al.* [2005] for an explicit definition of the Hall diffusion coefficient $d_{H\alpha}$). Neglecting displacement currents and applying the curl operator to Ampère's law gives:

$$\nabla^2 \mathbf{B} = -\mu_0 \nabla \times \mathbf{J}. \quad (2)$$

Equation (2) represents a set of three independent partial differential equations for B_L, B_ϕ, and $B_\parallel$. These were solved by applying Neumann boundary conditions and using the BiCGStab method in a manner similar to the electrostatic potential described above. After the computation of the magnetic field, a consistency check with the current system was performed using equation (2) to verify agreement.

3.2. Model Results

[11] Figure 2 shows representative diagnostic information for 10:24 UT. Figure 2a shows the plasma number density. By this time, plasma irregularities, spaced by 100–200 km, had reached the top of the simulation.

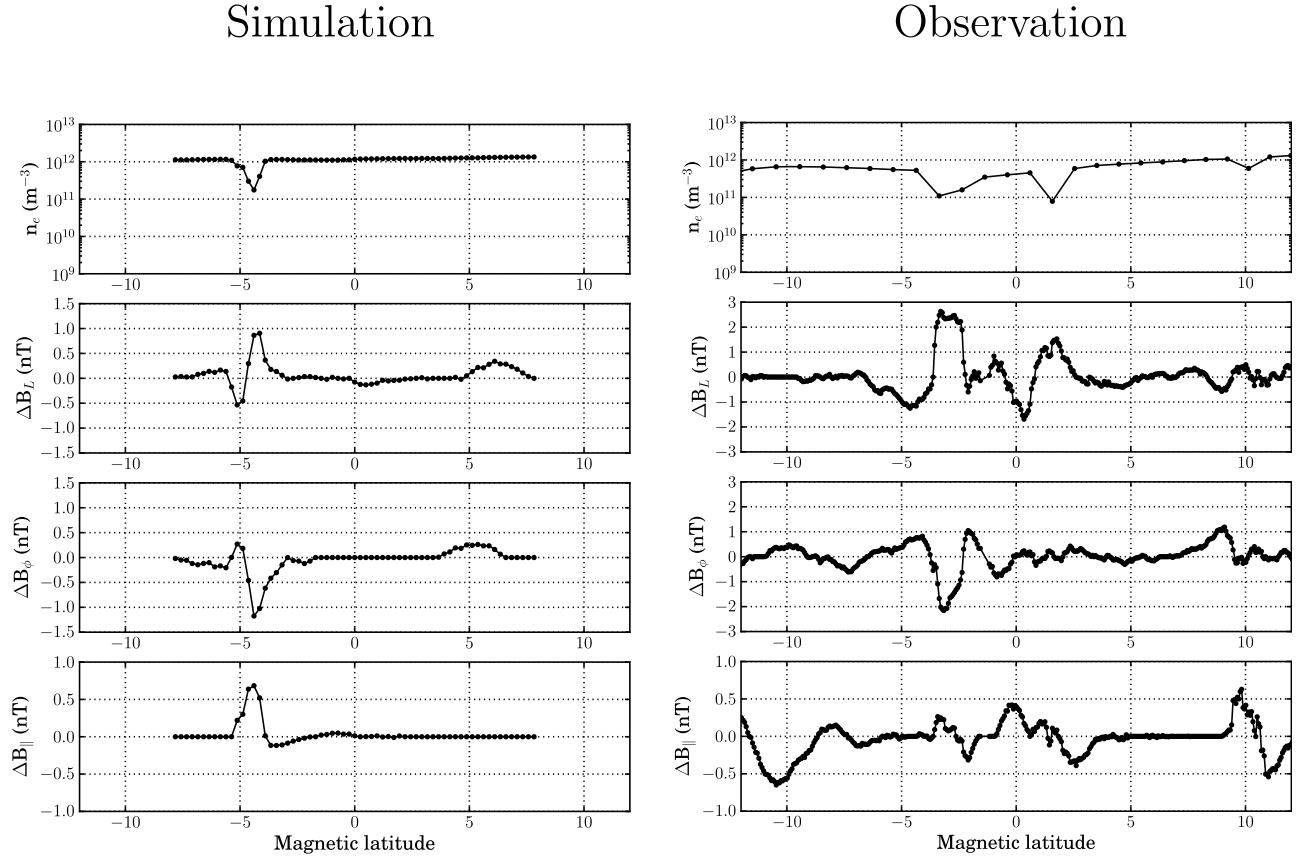

Figure 3. (left) Simulated satellite observations for August 11, 2004 at 10:24 UT, and (right) CHAMP observations for August 11, 2004, 10:00 UT: (top) plasma density, (middle top) meridional, (middle bottom) zonal, and (bottom) parallel magnetic field perturbations.

[12] The right-top color scale is used to indicate the magnitude and direction of the transverse current densities (scale maximum is 20 nA/m^2) and transverse magnetic induction (scale maximum is 3 nT). Figure 2c shows the transverse current density in the equatorial plane. Diamagnetic currents are observed flowing on the external walls of the plasma depletions in a clockwise direction. If evaluated together with Figure 2d, which indicates parallel magnetic inductions due to ionospheric currents, it can be seen that the currents caused northward deflections of $B_\parallel$ inside the plasma irregularities.

[13] Figures 2e and 2g display the parallel currents at conjugate points ±4° mag. latitude, respectivelly, north and south of the magnetic equator. The panels next to the parallel currents indicate the associated transverse magnetic inductions. FAC flow poleward (equatorward) on the external west (east) walls of the plasma depletions. Transverse magnetic induction showed a downward (upward) deflection inside the depletions north (south) of the magnetic equator. Transverse magnetic perturbations were negligible in the equatorial plane due to very small FAC and are not shown. The parallel current pattern observed in the simulations agrees with the schematic view in Figure 12 of *Stolle et al.* [2006].

3.3. Simulation Versus Satellite Comparisons

[14] Had a satellite passed through the simulated ionosphere at 380 km altitude over the Kwajalein sector at about 10:24 UT, the electron density and magnetic field perturbations would have appeared as shown in Figure 3 (left). Magnetic field data were high-pass filtered by a median filter (~700 km) to remove large-scale variations. The simulated results show a plasma depletion at ~−5° mag. latitude, collocated with an upward/westward $\Delta B_\perp$ of ~1.4 nT and a northward $\Delta B_\parallel$ of ~0.7 nT. A smaller transverse perturbation in the opposite direction (downward/eastward) was also detected next to the eastern wall of the plasma depletion.

[15] To compare the computed magnetic field inductions with observations, we used *in situ* magnetic field and plasma density measurements made by a Fluxgate Magnetometer (cross-calibrated with an Overhauser Magnetometer) and a Plasma Langmuir Probe on board the Challenging Minisatellite Payload (CHAMP). The satellite operated from July, 2000, to September, 2010, for studies related to the gravity field, geomagnetic field, and the atmosphere [*Lühr et al.*, 2002]. The satellite orbit altitude was about 380 km in 2004, inclined by 87.3° with respect to the equatorial plane, i.e., the orbit track was nearly parallel to the geographic meridian.

[16] Following *Park et al.*'s [2009] and *Stolle et al.*'s [2006] methodology, non-ionospheric contributions were removed from magnetic field measurements. The residual fields were further filtered by a 91-point median filter (~700 km) to remove large-scale variations. The final results represent short-scale deviations from the average magnetic

field. Figure 3 (right) displays CHAMP observations for August 11, 2004, by 10:00 UT, approximately at 178° geographic longitude. Since the satellite flew northward, when crossing a plasma depletion, the eastern wall is sampled first (due to the orbit inclination angle with respect to the magnetic flux tube in this longitude sector). The measurements indicated three main depletions in the plasma density (at magnetic latitudes ~−4°, 2°, and 10°). The depletion south of the magnetic equator (−4° mag. latitude) is collocated with magnetic perturbations in both the meridional and zonal components. The large upward deflection of the magnetic field inside the plasma depletion indicates a poleward (equatorward) current flowing on the external edge of the western (eastern) wall. The westward deflection of the magnetic field inside the depletion may be due to westward tilt of the ESF (as shown in Figures 2e and 2g). Finally, collocated with the plasma depletions, northward deflections of the magnetic field were detected. Note that the magnetic perturbation pattern observed by CHAMP is similar to the result obtained by the satellite pass simulation.

4. Discussions and Summary

[17] A three-dimensional numerical simulation of plasma density irregularities in the postsunset equatorial *F* region ionosphere leading to equatorial spread *F* (ESF) was performed to investigate the closure of ionospheric currents in the presence of plasma depletions. The simulation produced growing waveforms with characteristics that matched the observations made by ALTAIR radar, both in terms of their gross morphology and their rates of development.

[18] Overall, the simulated magnetic field perturbations show good qualitative with the CHAMP measurements. The simulation reproduces the main features of the plasma depletions as derived in a statistical study by *Park et al.* [2009], e.g., upward (downward) currents on their external western (eastern) edges. The field-aligned currents (FAC) showed large amplitudes associated with the divergence of the (mainly gravity-driven) zonal current at *F* region altitudes in the presence of ESF. FAC flow poleward (equatorward) on the external edges of the western (eastern) walls of the plasma depletions, i.e., strong FAC are associated with transverse currents closing around deep density depletions.

[19] We find that the transverse magnetic field perturbations are due almost entirely to FAC, whereas the parallel perturbations are due almost entirely to diamagnetic currents. Other currents (e.g., Pedersen and Hall) seem to make only minor contributions. That the simulation is electrostatic argues against an Alfvénic interpretation of all of the CHAMP magnetic field observations in ESF.

[20] **Acknowledgments.** HCA thanks C. Stolle for helpful discussions regarding field-aligned currents and equatorial spread *F*. This work was supported by award FA9550-09-1-0337 from the Air Force Office of Sponsored Research to Cornell University.

[21] The Editor thanks Arthur D. Richmond and an anonymous reviewer for their assistance in evaluating this paper.

References

Aggson, T. L., W. J. Burke, N. C. Maynard, W. B. Hanson, P. C. Anderson, J. A. Slavin, W. R. Hoegy, and J. L. Saba (1992), Equatorial bubbles updrafting at supersonic speeds, *J. Geophys. Res.*, *97*, 8581–8590.

Aveiro, H. C., and D. L. Hysell (2010), Three-dimensional numerical simulation of equatorial *F* region plasma irregularities with bottomside shear flow, *J. Geophys. Res.*, *115*, A11321, doi:10.1029/2010JA015602.

Bhattacharyya, A., and W. J. Burke (2000), A transmission line analogy for the development of equatorial ionospheric bubbles, *J. Geophys. Res.*, *105*, 24,941–24,950.

Hysell, D. L., M. F. Larsen, C. M. Swenson, and T. F. Wheeler (2006), Shear flow effects at the onset of equatorial spread *F*, *J. Geophys. Res.*, *111*, A11317, doi:10.1029/2006JA011963.

Koons, H. C., J. L. Roeder, and P. Rodriguez (1997), Plasma waves observed inside plasma bubbles in the equatorial *F* region, *J. Geophys. Res.*, *102*, 4577–4583.

Lühr, H., S. Maus, M. Rother, and D. Cooke (2002), First in-situ observation of night-time *F* region currents with the CHAMP satellite, *Geophys. Res. Lett.*, *29*(10), 1489, doi:10.1029/2001GL013845.

Park, J., H. Lühr, C. Stolle, M. Rother, K. W. Min, and I. Michaelis (2009), The characteristics of field-aligned currents associates with equatorial plasma bubbles as observed by the CHAMP satellite, *Ann. Geophys.*, *27*, 2685–2697.

Pottelette, R., M. Malingre, J. J. Berthelier, E. Seran, and M. Parrot (2007), Filamentary Alfvénic structures excited at the edges of equatorial plasma bubbles, *Ann. Geophys.*, *25*, 2159–2165.

Saad, Y. (1990), SPARSKIT: A basic tool kit for sparse matrix computations, *Tech. Rep. RIACS-90-20*, Res. Inst. for Adv. Comput. Sci., NASA Ames Res. Cent., Moffett Field, Calif.

Scherliess, L., and B. G. Fejer (1999), Radar and satellite global equatorial *F* region vertical drift model, *J. Geophys. Res.*, *104*, 6829–6842.

Shume, E. B., D. L. Hysell, and J. L. Chau (2005), Zonal wind velocity profiles in the equatorial electrojet derived from phase velocities of type II radar echoes, *J. Geophys. Res.*, *110*, A12308, doi:10.1029/2005JA011210.

Stolle, C., H. Lühr, M. Rother, and G. Balasis (2006), Magnetic signatures of equatorial spread *F* as observed by the CHAMP satellite, *J. Geophys. Res.*, *111*, A02304, doi:10.1029/2005JA011184.

Trac, H., and U. L. Pen (2003), A primer on Eulerian computational fluid dynamics for astrophysicists, *Astrophysics*, *115*, 303–321.

Woodman, R. F. (2009), Spread F—An old equatorial aeronomy problem finally resolved?, *Ann. Geophys.*, *27*, 1915–1934.

H. C. Aveiro and D. L. Hysell, Earth and Atmospheric Sciences, Cornell University, 2122 Snee Hall, Ithaca, NY 14853, USA. (hca24@cornell.edu)

H. Lühr and J. Park, Helmholtz Center Potsdam, GFZ German Research Center for Geosciences, Telegrafenberg, D-14473 Potsdam, Germany.